

2016-10-15

Annual down-glacier drainage of lakes and water-filled crevasses at Helheim Glacier, southeast Greenland

Everett, A

<http://hdl.handle.net/10026.1/8104>

10.1002/2016JF003831

Journal of Geophysical Research: Earth Surface

American Geophysical Union (AGU)

All content in PEARL is protected by copyright law. Author manuscripts are made available in accordance with publisher policies. Please cite only the published version using the details provided on the item record or document. In the absence of an open licence (e.g. Creative Commons), permissions for further reuse of content should be sought from the publisher or author.

1 Annual down-glacier drainage of lakes and
2 water-filled crevasses at Helheim Glacier, south east
3 Greenland

A. Everett¹, T. Murray¹, N. Selmes¹, I. C. Rutt¹, A. Luckman¹, T. D. James¹,
C. Clason³, M. O'Leary¹, H. Karunarathna², V. Moloney², D. E. Reeve²

Corresponding author: A. Everett, Glaciology Group, College of Science, Swansea University,
Swansea, UK (A.Everett.743498@Swansea.ac.uk)

¹Glaciology Group, College of Science,
Swansea University, UK

²Energy & Environment Group, College
of Engineering, Swansea University, UK

³Department of Physical Geography and
Quaternary Geology, Stockholm University,
Stockholm, Sweden

Key Points.

- We observe a down-glacier order of filling and draining in water-filled crevasses at Helheim Glacier.
- A model of surface-melt-driven hydrofracture cannot satisfactorily explain the observed results.
- We propose a theory which does not rely on hydrofracture in order to explain the results.

4 **Abstract.** Supraglacial lake drainage events are common on the Green-
5 land Ice Sheet. Observations on the west coast typically show an up-glacier
6 progression of drainage as the annual melt extent spreads inland. We use a
7 suite of remote sensing and modelling techniques in order to study a series
8 of lakes and water-filled crevasses within 20 km of the terminus of Helheim
9 Glacier, south east Greenland. Automatic classification of surface water ar-
10 eas shows a down-glacier progression of drainage, which occurs in the ma-
11 jority of years between 2007 and 2014. We demonstrate that a linear elas-
12 tic fracture mechanics model can reliably predict the drainage of the upper-
13 most supraglacial lake in the system, but cannot explain the pattern of fill-
14 ing and draining observed in areas of surface water downstream. We propose
15 that the water levels in crevasses downstream of the supraglacial lake can
16 be explained by a transient high-pressure wave passing through the subglacial
17 system following the lake drainage. We support this hypothesis with anal-
18 ysis of the subglacial hydrological conditions, which can explain both the po-
19 sition and interannual variation in filling order of these crevasses. Similar be-
20 haviour has been observed in association with jökulhaups, surging glaciers

21 and Antarctic subglacial lakes, but has not previously been observed on ma-
22 jor outlets of the Greenland Ice Sheet. Our results suggest that the behaviour
23 of near-terminus supraglacial water bodies may differ considerably from the
24 observed behaviour of inland supraglacial lakes, with wide-ranging implica-
25 tions for our understanding of the hydrology and dynamics of tidewater glaciers.

1. Introduction

26 Research has shown that hydrofracture can easily force a crevasse to penetrate through
27 the full thickness of an ice sheet [*van der Veen*, 2007], rapidly transporting large volumes
28 of surface meltwater to the bed [*Das et al.*, 2008] and leading to increases in flow speed on
29 diurnal [e.g. *Shepherd et al.*, 2009] to seasonal [e.g. *Bartholomew et al.*, 2010] time-scales.
30 These increases in flow speed may be driven by high water pressures in the subglacial
31 system, which reduce basal friction and lead to rapid sliding [*Iken*, 1981; *Iken and Bind-*
32 *schadler*, 1986; *Meier et al.*, 1994]. This mechanism has been observed at Helheim Glacier,
33 where ice velocity lags surface meltwater production by one day [*Andersen et al.*, 2011],
34 as well as at tidewater glaciers on the west coast of Greenland [*Sole et al.*, 2011], and in
35 Alaska [*Kamb et al.*, 1994; *Oneel et al.*, 2001].

36 Supraglacial lakes are a common cause of hydrofracture, and a number of studies have
37 found links between supraglacial lake drainage and increases in flow speed [e.g. *Das et al.*,
38 2008; *Danielson and Sharp*, 2013; *Tedesco et al.*, 2013]. Supraglacial lakes are most com-
39 monly found in the south-western region of the Greenland Ice Sheet (GrIS), with only
40 2% of lakes by number occurring in the South East [*Selmes et al.*, 2011]. Studies and
41 modelling work on the behaviour of supraglacial lakes have therefore mainly focussed on
42 the South West [e.g. *Box and Ski*, 2007; *Banwell et al.*, 2013; *Clason et al.*, 2015]. Remote
43 sensing investigations in this region have found that supraglacial lakes typically drain at
44 progressively higher altitudes as the melt season progresses [*Sundal et al.*, 2009; *Doyle*
45 *et al.*, 2013; *Morriss et al.*, 2013], a process which has been reproduced in modelling work
46 [*Arnold et al.*, 2014; *Clason et al.*, 2015]. The up-glacier progression of drainage has also

47 been observed in the Canadian Arctic, where water-filled crevasses close to the terminus
48 of Belcher Glacier were observed to drain by hydrofracture much earlier in the melt season
49 than lakes at higher elevations [*Danielson and Sharp, 2013*].

50 Despite the observed links between lake drainages, basal water pressure and flow speed,
51 observations of the subglacial system following lake drainages are still limited, particu-
52 larly at tidewater glaciers. A substantial volume of work has investigated the subglacial
53 hydrology of land-terminating glaciers through observations [e.g. *Hubbard and Nienow,*
54 *1997; Bartholomew et al., 2010; Chandler et al., 2013; Cowton et al., 2013*] and modelling
55 [e.g. *Banwell et al., 2013; Dow et al., 2015*]. However, the subglacial systems of tidewater
56 glaciers are typically much more difficult to access using techniques such as boreholes,
57 which are not suitable for the highly crevassed surface of large tidewater glaciers. Further
58 observations are vital in order to better understand the dynamics of tidewater glaciers, as
59 well as ice-ocean interactions and the impact on fjord circulation [*Straneo et al., 2013*].

60 Here we present the results from a range of techniques which were used to observe and
61 model the growth and drainage of a supraglacial lake and water-filled crevasses at Helheim
62 Glacier, south east Greenland. The combination of techniques highlights an unusual
63 pattern of filling and draining of these areas of surface water, not typically observed on
64 the Greenland Ice Sheet. We attempt to model this behaviour using a linear elastic
65 fracture mechanics model, but find that this theory cannot explain the observations. We
66 therefore propose an alternate hypothesis which is supported by analysis of the basal
67 hydrological conditions in the Helheim catchment.

2. Methods

2.1. Tracking surface water

68 A combination of Landsat, MODIS and high-resolution aerial photography were used to
69 monitor the growth and drainage of a lake and water-filled crevasses close to the terminus
70 of Helheim Glacier (Figure 1).

71 The atmospherically corrected, 250 m resolution MODIS Terra MOD09 Level 2 Surface
72 Reflectance product [*MODIS Land Science Team*, 2015] was used to automatically classify
73 areas of surface water. Images were acquired from the Level-1 & Atmosphere Archive
74 and Distribution System (LAADS) Distributed Active Archive Center (DAAC) for the
75 period 20th May – 30th September for all years from 2007 to 2014. Images were filtered
76 using the ‘250 m Resolution Surface Reflectance Band Quality Description’ and the ‘1 km
77 Resolution Data State’, both produced during processing and supplied with imagery. Data
78 were strictly filtered to exclude any pixels which were not classified as ‘highest quality’
79 after processing. Pixels not identified as ‘highest quality’ include those with an acute
80 solar angle, noisy detector, or those that contain cloud or fall in the shadow of cloud.

81 The lake, L , and areas containing water-filled crevasses $W1$, $W2$ and $W3$ (Figure 1)
82 recur annually in the same positions; we therefore defined a number of pixel windows
83 within the MODIS images centred on these areas, which we were able to use for all years.
84 The sizes of the pixel windows are shown in Table 1. If any pixels within the windows
85 did not meet the filtering criteria the entire window was discarded so as to avoid any
86 contamination of the window. This strict filtering left between 62 and 104 high-quality
87 MODIS window images per year.

88 Water area was classified within pixel windows using an automatic algorithm. The
89 method used here took the mean reflectance of the pixel window, and any pixels with
90 reflectance values below a threshold of this mean were taken to contain water. The
91 thresholds and window sizes used here are shown in Table 1. This technique has been
92 widely used in previous work [e.g. *Box and Ski*, 2007; *Selmes et al.*, 2011] and is reliable
93 where there is a strong difference in reflectance between the ice and the water surface.
94 For area L , the window contained an area of dark-coloured ice which led to a strong bias
95 on the mean values from this window. Therefore, for this window only, we took the mean
96 value from an adjacent control window which fell entirely on the light-coloured ice.

97 In order to quantify the error in automatic classification, the lake area was manually
98 digitised from 30 m resolution Landsat 7 and 8 images. These images were acquired from
99 the US Geological Survey using the LandsatLook Viewer, for the same day as the auto-
100 matically classified MODIS images. From these images, 28 high-quality, coincident image
101 pairs were found between 2010 and 2014. Comparison of the areas from the automatic
102 and manual classifications gave an RMSE of 0.08 km^2 and an R^2 of 0.73, showing that the
103 automatic classification performed reliably.

104 The timing of maximum water area was picked automatically from the resulting time
105 series. The lake typically has a single distinct maximum in area each year, and is easily
106 identified. In some years $W1$, $W2$ and $W3$ have multiple maxima; in this situation the
107 first maximum following the lake drainage is picked.

108 **2.1.1. Estimating lake volume**

109 Aerial photographs collected when the lake water level was relatively low were used
110 to produce a digital elevation model (DEM) of the lake basin from which lake volume

111 was derived. The photographs were captured on 24 July 2007 using a fully calibrated,
112 aircraft-mounted Wild RC-10 Aviphot vertical aerial camera system and digitized with
113 a high precision scanner in order to maintain radiometric and geometric fidelity. Pho-
114 togrammetric processing was carried out in the SocetSET Photogrammetry Suite v.5.6
115 using ground control data extracted from a temporally coincident lidar DEM, as described
116 in *James et al.* [2006]. The photogrammetric adjustment yielded root mean square errors
117 in the adjusted ground control of 2.4 m in X and Y and 0.5 m in Z, which provides a good
118 estimate of any systematic errors. An initial DEM of the lake and surrounding area was
119 collected manually at a grid spacing of 50 m taking advantage of SocetSET's interactive
120 3D editing capabilities. This low resolution surface was used as a 'seed' surface to con-
121 strain the automated terrain extraction in SocetSET's NGATE module. The resulting
122 5 m resolution DEM was then manually edited where required to produce the final DEM.
123 Because the lake water was clear of sediment, features on the submerged lake bottom
124 were easily visible to the camera and thus the final high resolution DEM included the
125 submerged lake bottom. While there is a refraction error associated with DEM collection
126 through water, due the height of the aircraft and shallowness of the water these errors
127 were small relative to the total volume of the lake.

128 We identify the high water line of the lake in the imagery as a change in the ice surface
129 from smooth, white ice within the lake basin, which we interpret as having been sub-
130 merged; to rougher, darker ice, which characterises the surrounding area and does not
131 appear to have been submerged. The boundary roughly follows a line of constant eleva-
132 tion, and we therefore interpret this as the pre-drainage height of the lake in 2007, thus
133 allowing the lake volume and depth to be derived.

2.2. Hydrofracture Modelling

134 2.2.1. LEFM Model

135 A linear elastic fracture mechanics (LEFM) model [*van der Veen, 2007*] was used to
 136 estimate drainage times, assuming that hydrofracture is forced by surface runoff. Models
 137 based upon these equations have previously been used to model lake drainages [*Clason*
 138 *et al., 2012; Clason et al., 2015*] and have been compared to observed crevasse depths
 139 [*Mottram and Benn, 2009*].

140 The LEFM model calculates the net stress intensity factor, K_I , at the tip of a crevasse
 141 using

$$K_I = 1.12R_{xx}\sqrt{\pi d} - 0.683\rho_i g d^{1.5} + 0.683\rho_w g b^{1.5}, \quad (1)$$

142 where R_{xx} is the tensile stress at a given point, d is the crevasse depth, and b is the
 143 depth of water in the crevasse [*van der Veen, 2007*]. Ice density, ρ_i , water density, ρ_w ,
 144 and gravitational acceleration, g , take standard values of 917 kg m^{-3} , 1000 kg m^{-3} and
 145 9.81 m s^{-2} , respectively.

146 When the tip stress, K_I , reaches a critical fracture stress, K_{IC} , the fracture begins
 147 to propagate downwards. Equation 1 is then solved iteratively with d increased until
 148 $K_I < K_{IC}$ or the crevasse has reached the bed. Following *Clason et al. [2015]*, we used
 149 a K_{IC} value of $150 \text{ kPa m}^{1/2}$. The model was forced with surface stresses R_{xx} , derived
 150 through feature-tracking of SAR imagery, and water depth b , determined using modelled
 151 runoff and approximated crevasse geometries, both described in more detail below.

152 We ran the model on a 40 m resolution grid within a $24 \text{ km} \times 28 \text{ km}$ domain, covering
 153 the terminus of Helheim. Within the domain, Equation 1 was evaluated at each grid

154 square with a time step of one day. The model was initialised with zero water depth at
 155 the start of each year. Model spin-up occurs within the first timestep, when crevasses are
 156 allowed to penetrate to the depth resulting from the background stress field.

157 **2.2.2. Surface stresses**

158 Surface velocities were derived using feature tracking between a pair of TerraSAR-X
 159 Stripmap Mode SAR images from 24th July and 8th August 2013. The images were
 160 chosen to represent the typical spatial pattern of summer flow speeds across the region of
 161 interest. Features were matched by cross-correlation within image patches of 200×200
 162 pixels ($\sim 400 \times 400$ m) at a sampling interval of 20 pixels yielding a velocity grid with a
 163 resolution of 40 m.

164 The two-dimensional plane strain rate tensor $\dot{\epsilon}_{ij}$ was calculated from velocity compo-
 165 nents u_i and u_j using

$$\dot{\epsilon}_{ij} = \frac{1}{2} \left(\frac{\partial u_i}{\partial x_j} + \frac{\partial u_j}{\partial x_i} \right). \quad (2)$$

166 We then calculated the deviatoric strain rate tensor $\dot{\epsilon}'_{ij}$ as

$$\dot{\epsilon}'_{ij} = \dot{\epsilon}_{ij} - \frac{\dot{\epsilon}_{kk}}{2} \delta_{ij}. \quad (3)$$

167 The deviatoric strain rate tensor $\dot{\epsilon}'_{ij}$ is related to the Cauchy stress tensor σ_{ij} by an
 168 inverse form of the creep relation [Nye, 1957] as follows:

$$\sigma_{ij} = A^{-1/n} \dot{\epsilon}'_{ij}{}^{(1-n)/n}, \quad (4)$$

169 where A is a flow parameter primarily dependent on the temperature of the ice, and n is
 170 a creep exponent. $\dot{\epsilon}_E$ is the second invariant of the strain rate tensor, also known as the
 171 effective strain, calculated using

$$\dot{\epsilon}_E = \sqrt{\frac{1}{2} (\dot{\epsilon}_{xx}^2 + \dot{\epsilon}_{yy}^2) + \dot{\epsilon}_{xy}^2 + \dot{\epsilon}_{yx}^2}. \quad (5)$$

172 Here we assumed an ice temperature of -5°C , giving A a value of $9.3 \times 10^{-25} \text{ s}^{-1} \text{ Pa}^{-3}$
 173 [Cuffey and Paterson, 2010], and n takes a typical value of 3. These values are similar to
 174 those used by Clason *et al.* [2015] on the west of Greenland.

175 The von Mises stress (σ_v) was then calculated directly from the Cauchy stress tensor as

$$\sigma_v = \sqrt{\sigma_{xx}^2 - \sigma_{xx}\sigma_{yy} + \sigma_{yy}^2 + 3\sigma_{xy}^2}. \quad (6)$$

176 The resulting von Mises equivalent stress was used to represent the tensile stress R_{xx}
 177 in Equation 1. The von Mises stress has been shown to be reliable for predicting the
 178 failure of glacier ice by Vaughan [1993] and has been widely used since [e.g. Hubbard and
 179 Hubbard, 2000; Clason *et al.*, 2012; Albrecht and Levermann, 2014]. For the purposes
 180 of the model, the stresses can be assumed to be constant through the depth of the ice
 181 [van der Veen, 2007].

182 2.2.3. Surface runoff and flow routing

183 Daily runoff data were gathered from the MARv3.5.2 model forced with ERA-Interim
 184 Reanalysis data [Fettweis *et al.*, 2013]. An example of the runoff data averaged over the
 185 catchment of $W3$ is illustrated in supplementary Figure SXX. The runoff was routed to
 186 surface water areas identified from remote sensing data using a D-Infinity flow routing

187 algorithm [Tarboton, 1997]. The flow was routed over a DEM which was pit filled ev-
188 erywhere except for locations where water was observed on the surface, thus sinks could
189 only form in these areas. Without this assumption we see a more uniform distribution
190 of water on the ice surface and no cases of hydrofracture. Any runoff flowing into sinks
191 within a surface water area was added to the volume of water within that area. This
192 volume was then distributed evenly across grid squares within each surface water area.
193 The catchments and approximated flow path lengths are summarised in Table 2.

194 **2.2.4. Crevasse Geometry**

195 In order to calculate the water depth b required in Equation 1, some assumptions were
196 made about the geometry of the lake or crevasse being filled. We used the geometry
197 illustrated in Figure 2, where the water was allowed to fill a crevasse and any remaining
198 water pooled on the surface. Similarly to Clason *et al.* [2015], we used a crevasse width
199 w_c of 1 m, which is uniform with depth, and we set the length equal to the grid size, in
200 this case 40 m. The crevasse depth d was initialised with a depth of 1 metre. During the
201 first timestep the model was spun-up, allowing crevasses to penetrate to the depth driven
202 by the background tensile stress.

203 There is some uncertainty in the selection of the crevasse width. Based upon the work
204 of Krawczynski *et al.* [2009], a width of 1 m is a conservative estimate for the areas we are
205 studying, where the ice is around 1000 m deep and under moderate tensile stress gradients.
206 However, in order to address the uncertainty, sensitivity tests were carried out on a range
207 of values of the crevasse width. Varying the crevasse length has a similar impact to the
208 crevasse width as it effectively increases the volume of the crevasse.

209 **2.2.5. Model Limitations**

210 Two errors are introduced by the flow routing assumptions used here. Firstly, we do
211 not account for flow delay and retention in the catchment; potentially leading to an
212 assumption of early hydrofracture. However, as can be seen from Table 2, the catchments
213 are relatively small, average flow paths are up to 5.8 km for area *L* and much smaller
214 for other areas, and the catchments largely become snow free early in the melt season,
215 leading to minimal retention. The maximum flow path length is 12 km for area *W1*. Based
216 upon a conservative assumption that water travels at an average of 0.1 m s^{-1} within the
217 catchment, the maximum flow path of 12 km would only take around 36 hours drain to
218 the surface water areas. Therefore we expect this to have a minimal impact on the time
219 of hydrofracture. Secondly, by spreading the water volume evenly over the maximum
220 water area we underestimate the maximum water depth in the early stages of filling,
221 potentially leading to an assumption of later hydrofracture than in reality. This is therefore
222 a conservative assumption for the purposes of this model.

223 **2.2.6. Sensitivity Testing**

224 Sensitivity tests were carried out on an idealised model setup in order to isolate the
225 sensitivity of the model from spatial variability in the model forcings. Five key parameters
226 were tested, which are discussed individually below. The setup is forced with an idealised
227 runoff profile, illustrated in supplementary Figure SXX. The sensitivity tests were run
228 using a Monte Carlo method, where the likely range of each parameter was defined and
229 a different randomly selected value from within this range was used for each model run.
230 The probability distribution within each range was assumed to be uniform; however, as
231 some of the parameter ranges are skewed, an equal number of samples were selected from
232 above and below the base values. Two types of test were performed. In the first, a single

parameter was varied while all others were kept at their base values, thus allowing the sensitivity of the model to each individual parameter to be tested. In the second type of test, all parameters were varied simultaneously, allowing the overall uncertainty in the modelled time of drainage to be tested. In each test the model was run for 5000 different randomly selected parameter combinations. The range and base values of each parameter are discussed below and summarised in Table 3. The results are discussed and presented as the difference in days from the base case, and the interquartile range (IQR) is used as a metric to compare the relative sensitivity of the different parameters.

2.2.6.1. Runoff

The largest source of uncertainty in the runoff arises from the catchment delineation. Smaller catchments lead to later hydrofracture, up to a threshold where there is insufficient water for hydrofracture to occur. However, while small catchments may explain later hydrofracture, they cannot explain why water is only found in discrete areas on the surface of the glacier. Based upon these limitations we set the lower bound of the runoff as a 50% decrease in catchment area, and the upper bound as a doubling in catchment size. A multiplication factor α_f was used to alter the runoff in the model using values between 0.5 and 2, and a base value of 1.

The sensitivity tests show that the model is highly sensitive to the runoff, with the interquartile range (IQR) of the difference between modelled and observed results equal to 9 days, the second largest IQR of the parameters tested.

2.2.6.2. Crevasse Spacing

The effects of crevasse spacing were tested by *van der Veen* [1998] through modification of the tensile stress term in Equation 1 such that the first term becomes

$$K_I^{(1)} = D(S)R_{xx}\sqrt{\pi dS} \quad (7)$$

256 where S is the ratio of the crevasse spacing to the sum of the crevasse depth and the
 257 spacing, such that $S \rightarrow 0$ as the spacing decreases. $D(S)$ is then an empirical function of
 258 S which varies between 0.5 and 1.12. For the full definition of these factors see *van der*
 259 *Veen* [1998].

260 For the sensitivity tests performed here, a ratio of crevasse spacing to depth of 1:9 was
 261 taken as a lower bound estimate of the spacing at Helheim, giving S a value of 0.1. As
 262 crevasse spacing increases $S \rightarrow 1$, therefore $S = 1$ was taken as an upper bound on the
 263 range of S . In the absence of more detailed information, we also used $S = 1$ as the base
 264 value for other model runs, but as shown by the sensitivity results this had a minimal
 265 impact on the results.

266 The results of the sensitivity testing show that the model is insensitive to the crevasse
 267 spacing. The IQR of the parameters tested is 1 day, which is equal to the model timestep.
 268 Closer inspection of the model results shows that increased crevasse spacing leads to an
 269 increase in the initial crevasse depth forced by the background stress field, but once runoff
 270 is added hydrofracture occurs at much the same time.

271 **2.2.6.3. Tensile Stress**

272 The parameter space for the tensile stress was defined by allowing for errors in the
 273 selection of the value of A ; a temperature dependent flow parameter used in the creep
 274 relation (Equation 4). Previous work has assumed an ice temperature of -5°C [e.g. *Clason*
 275 *et al.*, 2012], which gives A a value of $9.3 \times 10^{-25} \text{ s}^{-1} \text{ Pa}^{-3}$ [*Cuffey and Paterson*, 2010]. We
 276 took the limits of our parameter space as 0°C and -30°C which give values of 2.4×10^{-24}

277 $\text{s}^{-1}\text{Pa}^{-3}$ and $3.7 \times 10^{-26} \text{ s}^{-1}\text{Pa}^{-3}$ for A , respectively. The effect of the choice of this pa-
278 rameter is to alter the mean stress in the catchment from 303 kPa at -5°C to 220 kPa and
279 889 kPa for 0°C and -30°C respectively. We therefore took these as the limits of our
280 parameter space in the Monte Carlo sensitivity testing, with a base value of 300 kPa.

281 Varying the tensile stress has a very similar impact to varying the crevasse spacing, in
282 that the size of the first term in Equation 1 is increased or decreased relative to the other
283 terms in the equation. It therefore has a similar impact on the modelled results; crevasses
284 penetrate deeper during spin-up, but the IQR of 1 day shows a very minor impact on the
285 day of hydrofracture.

286 **2.2.6.4. Critical Stress Factor**

287 Values of K_{IC} between 100 and 400 $\text{kPa m}^{1/2}$ were used by *van der Veen* [1998] based
288 upon previous laboratory testing of glacier ice (see *van der Veen* [1998] and references
289 therein). We extend this range to cover the values used by *Mottram and Benn* [2009] who
290 tested values as low as 10 $\text{kPa m}^{1/2}$, which may be more appropriate for weaker ice close to
291 the terminus of Helheim. The range of values for K_{IC} used here therefore cover the range
292 10 – 400 $\text{kPa m}^{1/2}$, with 150 kPa taken as a base value consistent with previous work.

293 Consistent with previous studies [*van der Veen*, 2007; *Scott et al.*, 2010; *Clason et al.*,
294 2012], the results of sensitivity testing show that the date of hydrofracture is insensitive
295 to the value of K_{IC} used in the model, with an IQR of 1 day.

296 **2.2.6.5. Crevasse Width**

297 Field measurements and observations of crevasse widths forced by hydrofracture are
298 limited. A maximum crevasse width of 0.4 m was measured by *Doyle et al.* [2013], following
299 hydrofracture of a lake on the west coast of Greenland. Further research by *Krawczynski*

300 *et al.* [2009] suggests that these widths may be up to 1–2 m for very deep cracks (> 1500 m)
 301 or for high longitudinal stress gradients. In order to capture this variation, we tested a
 302 range of values between 0.1 and 2 m, taking a base value of 1 m.

303 The results of sensitivity testing show that the model is very sensitive to crevasse width,
 304 with the highest IQR of 15 days. The results show a skew towards earlier hydrofracture,
 305 which occurs with reducing crevasse widths.

306 **2.2.6.6. Combined**

307 The combined sensitivity test allows all parameters to vary at random within the ranges
 308 defined above. This provides an estimate of the overall uncertainty in the model, and is
 309 used to define the error bars in results plots. For the combined test, the results show an
 310 IQR of 14 days. The 5th and 95th percentiles show that 90% of the model results lie
 311 within ± 15 days of the modelled date of hydrofracture. Given the wide ranges within
 312 which the parameters are allowed to vary, it is unlikely that the error of the model is
 313 outside this range.

2.3. Subglacial Hydrology

314 Hydraulic potential in Helheim catchment was calculated from the Greenland Mapping
 315 Project (GIMP) surface DEM [Howat *et al.*, 2014], and the IceBridge BedMachine Green-
 316 land Version 2 bed DEM [Morlighem *et al.*, 2014], both at a spatial resolution of 150 m.
 317 Based upon the work of Shreve [1972], the hydraulic potential, Φ , was calculated using

$$\Phi = k\rho_i g(h_s - h_b) + \rho_w g h_b, \quad (8)$$

318 where h_s and h_b are the surface and bed elevations, and k is a fraction of overburden
319 pressure, typically set to 1.0 based upon the assumption that the entire catchment is at
320 overburden pressure. We relaxed this assumption in order to test how variations in this
321 fraction affected the hydraulic potential within the catchment [*Lindbäck et al.*, 2015]. We
322 use values of k between 0.5 and 1.2 in order to test the likely range of basal effective
323 pressures.

324 In order to determine flow routing, the hydraulic potential surface was pit filled to
325 remove any sinks. Flow direction and flow accumulation were then calculated using a
326 D-Infinity flow algorithm [*Tarboton*, 1997].

3. Results

3.1. Remote Sensing

327 A summary of results from all years is shown in Figure 3, full results from the automatic
328 classification of surface water for all years are included in the supplementary material
329 (Figures S3 - S10). The filling and draining patterns of all water areas can be clearly
330 identified and variations in area are considerably larger than the errors associated with
331 the method. While there is considerable annual variability in the maximum area of water,
332 a number of clear patterns emerge. The most obvious is the consistent pattern of the
333 drainage of L preceding the filling and draining of $W1$, $W2$ and $W3$, all downstream and
334 at lower elevations. Typically, L drains between the 20th and 30th June, while $W1$, $W2$,
335 and $W3$ generally drain in early July. The maximum area of L ranges between 0.25 and
336 0.52 km^2 , with the maximum area of $0.52 \pm 0.08 \text{ km}^2$ observed in 2011. $W1$, $W2$ and $W3$
337 have areas ranging between 0 and 0.48 km^2 , with $W2$ and $W3$ usually larger than $W1$.

338 The one exception to the down-glacier progression of drainage is 2009, where we see
339 slow growth of L with the maximum area occurring after $W1$, $W2$ and $W3$ have drained.
340 The slow filling rate cannot be explained by lower runoff, as we see no significant differ-
341 ence in runoff volume when compared to other years (Figure S2). We therefore identify
342 two possible explanations for this; i) surface flow routing is different in 2009 and runoff
343 drains through a different connection to the bed rather than collecting in the lake, or ii)
344 hydrofracture creates a constricted connection to the bed allowing drainage at a rate less
345 than the input of surface runoff. Both would result in suppressed lake growth, but similar
346 behaviour to other years in $W1$, $W2$ and $W3$.

347 Figure 5 shows the 5 m resolution DEM produced from aerial photography. From the
348 DEM, the maximum volume of L is estimated to be $\sim 9.7 \times 10^6 \text{ m}^3$ in 2007. The moulin
349 down which the lake drained in 2007 is easily identifiable to the south east of the lake.
350 It is notable that in 2007 the lake is split by an ice divide, which is crossed by a narrow
351 channel, while this would still allow the majority of water to drain from the lake, it may
352 slow the rate of drainage.

3.2. Hydrofracture Modelling

353 The results of the LEFM modelling are illustrated in Figure 3, alongside the observed
354 results. Figure 4 divides the results by area and more clearly shows the relationship, or
355 lack of, between observed and modelled results.

356 The model consistently predicts the drainage of the lake L within 2 days of the obser-
357 vations, with the only outliers being 2009, which has been discussed previously, and 2010,
358 which the model also slightly underestimates. The RMSE of the difference between the
359 modelled results and observations for L is 4.31 days, showing that the model performs

360 reliably for this area. However, the results for the lower water areas show much less con-
361 sistency; RMSEs are 24.93, 13.01 and 15.64 days for areas $W1$, $W2$ and $W3$, respectively.
362 For $W1$ all observed dates of hydrofracture lie above the 95th percentile of the modelled
363 results, implying that both runoff and crevasse width must be at the extremities of their
364 parameter ranges in order to match the observations. The results for $W2$ and $W3$ are
365 slightly more consistent, but still 2 out of 8 results are above the 95th percentile for $W2$
366 and 5 out of 8 for $W3$. The relationship between modelled and observed results for L ,
367 which is not present in areas $W1$, $W2$ or $W3$, is clearly illustrated in Figure 4. While the
368 difference in an individual year could be attributed to uncertainty in parameter choices,
369 there is no consistency in this difference by area or by year. The lack of a relationship in
370 the results would therefore require a different parameter selection for each year and area
371 in order to see better agreement between modelled and observed results.

3.3. Subglacial Hydrology

372 Figure 6 shows contours of hydraulic potential calculated assuming that the fraction of
373 overburden k is equal to 1.0. The locations of water-filled crevasses, identified in Figure
374 1, coincide closely with sinks and areas of convergence in the hydraulic potential.

375 Two flow accumulation maps, calculated from the hydraulic potential, are also shown
376 in Figure 6. These are calculated using values for overburden fractions of 1.00 and 1.14.
377 The full range of values $0.5 < k < 1.2$ are presented in supplementary video SXX. Figure
378 6 and the supplementary video both highlight the dramatic changes in flow switching
379 which occur at different values of the overburden fraction k . At low values of k , the steep
380 gradient of the hydraulic potential drives water into the central parts of the glacier. The
381 water areas are located within a few hundred metres of the flow paths, but may not be

382 directly connected to the subglacial flow routing. As k increases the hydraulic potential
383 gradient begins to get less steep. Flow paths migrate towards the locations of surface
384 water, with a switch connecting areas $W2$ and $W3$ around $k = 0.97$. Above $k = 1$ all
385 areas of surface water appear to be connected, but are not in a down-stream order until a
386 major switch between areas $W1$ and $W2$ around $k = 1.13$. A number of rapid switches in
387 flow routing occur when $k > 1$; as the gradient of the hydraulic potential gets shallower,
388 rapid flow switching appears more likely to occur.

389 This is a major simplification of a highly complex system, but it is illustrative of the
390 rapid switching which can occur with changes in basal effective pressure. We also note
391 that values of k will vary across the catchment, rather than the uniform values used here;
392 therefore, the calculated flow routing indicates that in different years, and even within the
393 same year, we would expect to see the flow routed in different ways within the catchment.

4. Discussion

394 The down-glacier progression of drainage observed in remote sensing data is unusual,
395 and contrary to the results of *Sundal et al.* [2009] and *Danielson and Sharp* [2013], who
396 saw the order of drainage progressing up-stream as the seasonal melt extent spread inland.
397 The observations are particularly significant as the pattern is seen to occur in the majority
398 of years between 2007 and 2014.

399 The observations could simply be explained by water draining over the surface of the
400 glacier between water areas. However, we can clearly identify a moulin following the
401 lake drainage from both Figure 5 and handheld photography collected in other years;
402 this indicates that water is draining to either the subglacial or the englacial system rather
403 than over the surface. While englacial drainage is a possibility, the highly stressed, heavily

404 crevassed conditions at Helheim make it unlikely that water would flow for more than a few
405 kilometers without encountering existing fractures or weaknesses allowing access to the
406 bed. Additionally, the work of *Andersen et al.* [2011] suggests efficient drainage between
407 the surface and the bed, implying that water is not retained in a complex englacial system.

408 We attempted to explain the order of drainage with variations in surface melt and
409 catchment size using a LEFM model. The model correctly predicts the date of drainage
410 of the lake L within a few days for the majority of years (RMSE = 4.3 days), however,
411 the results for the lower areas show much less consistency with the observations (RMSE
412 > 13 days). Sensitivity testing of the model shows that changes in two parameters, the
413 runoff and crevasse width, could account for the difference between observed and modelled
414 results.

415 While the change in crevasse width could account for the difference between modelled
416 and observed results in an individual year, it cannot account for the variability in the
417 difference from year to year. Uncertainty in the crevasse width can largely be attributed
418 to uncertainty in the shear modulus of ice [*Krawczynski et al.*, 2009, Figure 1]. Any error
419 in the estimation of the shear modulus would introduce a systematic bias to the results
420 which would lead to a consistent over- or under-estimation of the results. However, in
421 order to explain the interannual variation in the difference between observed and modelled
422 results, the shear modulus of the ice would have to vary by an order of magnitude from
423 year to year. Variations in the tensile stress also affect the crevasse width, but on the
424 order of 0.1 m per year [*Krawczynski et al.*, 2009, Figure 1], which could not account for
425 the interannual variability between observed and modelled results. It therefore seems

426 unlikely that the uncertainty in crevasse width could explain the interannual variability
427 of the difference between modelled and observed results.

428 Therefore, the only parameter which would be responsible for the interannual variation
429 in hydrofracture appears to be the runoff. However, for runoff to account for the difference
430 in the modelled and observed drainage times, catchment sizes would have to fluctuate in
431 area by $\pm 20\text{--}80\%$ from year to year. The resulting changes in catchment size would lead
432 to dramatically different patterns of surface water in different years. Years with small
433 catchment areas would show a much more distributed pattern of water on the surface of
434 the glacier than in years with large catchments. However, the observations show no such
435 patterns. The variation in catchment size necessary to explain this variability is therefore
436 difficult to reconcile with observations at Helheim, particularly the consistent locations
437 and distributions of surface water. This evidence strongly suggests that hydrofracture is
438 not the cause of the observed pattern of filling and draining at Helheim.

439 We therefore propose an alternate explanation which does not rely upon hydrofracture.
440 We suggest that the down-glacier order of filling and draining can be explained by a high-
441 pressure wave propagating down glacier following the lake drainage, controlling surface
442 water levels as it passes. Transient high-pressure waves such as this have been theorised
443 and observed in association with jökulhlaups [*Walder and Driedger, 1995; Tweed and*
444 *Russell, 1999*], producing pressures sufficient to flood the surface in areas of weakness
445 [*Tweed and Russell, 1999; Jóhannesson, 2009*], and also during surges [e.g. *Kamb et al.,*
446 *1985; Fowler et al., 2001*]. The propagation speed of the inferred pressure wave at Helheim
447 is an order of magnitude lower than those observed in jökulhlaups; but drainages rates
448 are similar to those observed in Antarctic lakes, where lower pressure gradients were

449 thought to limit the rate of drainage [*Fricke et al.*, 2007]. The system may therefore
450 be more analogous to the sequential filling and draining of subglacial lakes observed in
451 Antarctica [*Fricke et al.*, 2016], with the weaker, more heavily crevassed terminus at
452 Helheim allowing high basal water pressures to flood the surface, rather than raising the
453 ice.

454 Modelling studies have indicated that pressures above overburden can be sustained for
455 between 4 days and 4 weeks, and typically occur between late June and early July on
456 the west coast of Greenland [*Banwell et al.*, 2013; *Dow et al.*, 2015]. Such pressures have
457 been observed previously on the GrIS [*Cowton et al.*, 2013; *Meierbachtol et al.*, 2013],
458 but rarely for periods of more than a few days. We suggest that the early season lake
459 drainage transfers a large volume of meltwater into an inefficient winter arrangement of
460 the subglacial system. The water is supplied at a rate sufficient to overcome the capacity
461 of the existing subglacial system and forces the propagation of a high pressure wave down-
462 glacier as the system capacity increases. The observations and timescales show excellent
463 consistency with the sustained high pressures observed by *Banwell et al.* [2013] in their
464 modelling results.

465 Previous work on jökulhlaups has identified basal water flooding the surface. However,
466 in Landsat imagery from 2015, the water visible in crevasses at Helheim has spectral
467 characteristics more similar to isolated supraglacial lakes than to the turbid water seen in
468 plumes and marginal water bodies. This suggests that while high basal water pressures
469 may control water levels, the water visible on the surface is more likely surface melt which
470 is prevented from draining through the crevasses by high basal water pressure. However,
471 we note that *Andersen et al.* [2011] did observe turbid water upwelling into an open relict-

472 moulin structure just behind the calving front at Helheim, clearly showing that pressures
473 sufficient for basal water to reach the surface can and do occur. The LEFM modelling
474 work indicates a way by which a hydraulic connection between the surface and the bed
475 could be created in the necessary areas during the early melt season. Alternatively, basal
476 water pressures may be sufficient to fill or open existing fractures, as appears to have
477 happened in the 1996 Grimsvötn jökulhlaup [*Jóhannesson, 2009*].

478 Further support for this hypothesis is provided by the hydraulic potential and flow
479 routing results. Figure 6 shows that water-filled crevasses appear in points of convergence
480 and depressions in the hydraulic potential surface, particularly at higher values of k ,
481 which would be expected following a lake drainage. We acknowledge that the hydraulic
482 potential at the bed is strongly influenced by surface slope, and it is therefore difficult
483 to distinguish which is causing the water to collect in these areas. However, as we have
484 highlighted previously, the surface of Helheim is heavily crevassed and we see no evidence
485 for significant flow over the surface of the glacier which would lead water to collect in
486 these areas. The positions of the water areas are therefore consistent with where water
487 might be expected to collect if it were forced by conditions at the bed.

488 Figure 6 also shows dramatic variations in flow routing within the catchment when
489 the basal water pressure is at different fractions of overburden, consistent with the work
490 of *Lindbäck et al.* [2015]. As values of the overburden fraction k vary spatially and
491 temporally within the catchment, the differences identified in both the order of filling
492 and maximum extent of water areas can be explained by spatial and temporal variations
493 of k . The flow switching in the catchment which connects all areas in a down-stream
494 order occurs within a few kilometers of the lake, within the region where uplift has been

495 observed following previous lake drainages [*Das et al.*, 2008; *Doyle et al.*, 2013; *Tedesco*
496 *et al.*, 2013]. It is therefore quite probable that basal effective pressures reach the necessary
497 values in this region for water to cross the catchment and connect to other areas of surface
498 water downstream. In future, it may be possible to identify the flow routing regime and
499 overburden pressures from more detailed study of these water areas. However, for the
500 present we simply take this as evidence to explain the variability in timing of the filling
501 and draining of the water-filled crevasses.

502 Our hypothesis is therefore consistent with evidence from the basal hydrological con-
503 ditions at Helheim, and we believe this warrants further investigation in order to better
504 understand the processes controlling the observed behaviour.

5. Conclusion

505 We have observed an unusual pattern of growth and drainage of a lake and water-filled
506 crevasses near the terminus of Helheim Glacier, south east Greenland, which is consistent
507 over an eight year period. A combination of remote sensing observations and modelling
508 have been used to demonstrate that hydrofracture is unlikely to explain the observed
509 behaviour. We therefore presented a new hypothesis for a transient high-pressure wave
510 propagating down glacier following the lake drainage. We suggest that water pressures
511 in the subglacial system can control surface water levels through a hydraulic connection
512 to the bed caused by early season hydrofracture or pre-existing fractures in the ice. We
513 have supported our hypothesis with evidence from hydraulic potential maps of Helheim
514 catchment, which explain the observed positions of water-filled crevasses, and estimates of
515 flow routing, which explain the inter-annual variation in the order of filling and draining

516 of these water areas. This is an interesting and intriguing phenomenon, which certainly
517 warrants further investigation.

518 The system has similarities to pressure waves observed during surges and following
519 jökulhlaup floods, and also to the sequential order of filling and draining observed in
520 Antarctic subglacial lakes. However, none of these behaviours have previously been iden-
521 tified on the GrIS. Therefore, if true, this may have major implications for our under-
522 standing of the subglacial hydrology of tidewater glaciers, especially in relation to the
523 impacts of near-terminus lake drainage events.

524 We have demonstrated that remote sensing observations can resolve the fluctuations
525 in surface water area. If the link to the basal hydrological system can be verified, this
526 technique maybe provide a unique and easily obtainable insight into the subglacial hy-
527 drological system which could complement other techniques such as boreholes and dye
528 tracing.

529 We expect that investigation of other tidewater glaciers may provide evidence of sim-
530 ilar processes elsewhere. Further field investigations will improve our understanding of
531 the observed behaviour and provide valuable insight into the subglacial hydrology and
532 dynamics of tidewater glaciers.

533 **Acknowledgments.**

534 AE and VM are supported by Swansea University Scholarships. Aerial photographs and
535 lidar were collected by the NERC Airborne Remote Sensing Facility. TerraSAR-X data
536 were provided by DLR under project number HYD0178. We also thank Tim Bartholomäus
537 and two anonymous reviewers whose comments greatly improved this paper.

References

- 538 Albrecht, T., and A. Levermann (2014), Fracture-induced softening for large-scale ice
539 dynamics, *The Cryosphere*, *8*(2), 587–605, doi:10.5194/tc-8-587-2014.
- 540 Andersen, M., M. Nettles, P. Elosegui, T. Larsen, G. Hamilton, and L. Stearns
541 (2011), Quantitative estimates of velocity sensitivity to surface melt variations at
542 a large Greenland outlet glacier, *Journal of Glaciology*, *57*(204), 609–620, doi:
543 10.3189/002214311797409785.
- 544 Arnold, N. S., A. F. Banwell, and I. C. Willis (2014), High-resolution modelling of the
545 seasonal evolution of surface water storage on the Greenland Ice Sheet, *The Cryosphere*,
546 *8*(4), 1149–1160, doi:10.5194/tc-8-1149-2014.
- 547 Banwell, A. F., I. C. Willis, and N. S. Arnold (2013), Modeling subglacial water routing
548 at Paakitsoq, W Greenland, *J. Geophys. Res. Earth Surf.*, *118*(3), 1282–1295, doi:
549 10.1002/jgrf.20093.
- 550 Bartholomew, I., P. Nienow, D. Mair, A. Hubbard, M. A. King, and A. Sole (2010),
551 Seasonal evolution of subglacial drainage and acceleration in a Greenland outlet glacier,
552 *Nature Geoscience*, *3*(6), 408–411, doi:10.1038/ngeo863.
- 553 Box, J. E., and K. Ski (2007), Remote sounding of Greenland supraglacial melt lakes:
554 implications for subglacial hydraulics, *Journal of Glaciology*, *53*(181), 257–265, doi:
555 10.3189/172756507782202883.
- 556 Chandler, D. M., J. L. Wadham, G. P. Lis, T. Cowton, A. Sole, I. Bartholomew, J. Telling,
557 P. Nienow, E. B. Bagshaw, D. Mair, S. Vinen, and A. Hubbard (2013), Evolution of the
558 subglacial drainage system beneath the Greenland Ice Sheet revealed by tracers, *Nature*
559 *Geoscience*, *6*, 195–198, doi:10.1038/ngeo1737.

- 560 Clason, C., D. W. F. Mair, D. O. Burgess, and P. W. Nienow (2012), Modelling the
561 delivery of supraglacial meltwater to the ice/bed interface: application to south-
562 west Devon Ice Cap, Nunavut, Canada, *Journal of Glaciology*, *58*, 361–374, doi:
563 10.3189/2012JoG11J129.
- 564 Clason, C. C., D. W. F. Mair, P. W. Nienow, I. D. Bartholomew, A. Sole, S. Palmer, and
565 W. Schwanghart (2015), Modelling the transfer of supraglacial meltwater to the bed of
566 Leverett Glacier, Southwest Greenland, *The Cryosphere*, *9*(1), 123–138, doi:10.5194/tc-
567 9-123-2015.
- 568 Cowton, T., P. Nienow, A. Sole, J. Wadham, G. Lis, I. Bartholomew, D. Mair, and
569 D. Chandler (2013), Evolution of drainage system morphology at a land-terminating
570 Greenlandic outlet glacier, *Journal of Geophysical Research (Earth Surface)*, *118*, 29–41,
571 doi:10.1029/2012JF002540.
- 572 Cuffey, K. M., and W. S. B. Paterson (2010), *The Physics of Glaciers, Fourth Edition*,
573 Academic Press.
- 574 Danielson, B., and M. Sharp (2013), Development and application of a time-lapse photo-
575 graph analysis method to investigate the link between tidewater glacier flow variations
576 and supraglacial lake drainage events, *Journal of Glaciology*, *59*(214), 287–302, doi:
577 10.3189/2013jog12j108.
- 578 Das, S. B., I. Joughin, M. D. Behn, I. M. Howat, M. A. King, D. Lizarralde, and M. P.
579 Bhatia (2008), Fracture propagation to the base of the Greenland ice sheet during
580 supraglacial lake drainage, *Science*, *320*(5877), 778–781, doi:10.1126/science.1153360.
- 581 Dow, C. F., B. Kulesa, I. C. Rutt, V. C. Tsai, S. Pimentel, S. H. Doyle, D. As,
582 K. Lindbäck, R. Pettersson, G. A. Jones, and A. Hubbard (2015), Modeling of sub-

583 glacial hydrological development following rapid supraglacial lake drainage, *Journal of*
584 *Geophysical Research (Earth Surface)*, 120, 1127–1147, doi:10.1002/2014JF003333.

585 Doyle, S. H., A. L. Hubbard, C. F. Dow, G. A. Jones, A. Fitzpatrick, A. Gusmeroli,
586 B. Kulesa, K. Lindback, R. Pettersson, and J. E. Box (2013), Ice tectonic deformation
587 during the rapid in situ drainage of a supraglacial lake on the Greenland Ice Sheet, *The*
588 *Cryosphere*, 7(1), 129–140, doi:10.5194/tc-7-129-2013.

589 Fettweis, X., B. Franco, M. Tedesco, J. H. van Angelen, J. T. M. Lenaerts, M. R. van den
590 Broeke, and H. Gallée (2013), Estimating the Greenland ice sheet surface mass balance
591 contribution to future sea level rise using the regional atmospheric climate model MAR,
592 *The Cryosphere*, 7(2), 469–489, doi:10.5194/tc-7-469-2013.

593 Fowler, A., T. Murray, and F. Ng (2001), Thermally controlled glacier surging, *Journal*
594 *of Glaciology*, 47(159), 527–538, doi:10.3189/172756501781831792.

595 Fricker, H. A., T. Scambos, R. Bindshadler, and L. Padman (2007), An Active Subglacial
596 Water System in West Antarctica Mapped from Space, *Science*, 315(5818), 1544–1548,
597 doi:10.1126/science.1136897.

598 Fricker, H. A., M. R. Siegfried, S. P. Carter, and T. A. Scambos (2016), A decade of
599 progress in observing and modelling Antarctic subglacial water systems, *Phil. Trans.*
600 *R. Soc. A*, 374(2059), 20140,294, doi:10.1098/rsta.2014.0294.

601 Howat, I. M., A. Negrete, and B. E. Smith (2014), The Greenland Ice Mapping Project
602 (GIMP) land classification and surface elevation data sets, *The Cryosphere*, 8(4), 1509–
603 1518, doi:10.5194/tc-8-1509-2014.

604 Hubbard, A., and B. Hubbard (2000), The potential contribution of high-resolution glacier
605 flow modelling to structural glaciology, *Geological Society, London, Special Publications*,

- 606 176(1), 135–146, doi:10.1144/gsl.sp.2000.176.01.10.
- 607 Hubbard, B., and P. Nienow (1997), Alpine subglacial hydrology, *Quaternary Science*
608 *Reviews*, 16(9), 939–955, doi:10.1016/s0277-3791(97)00031-0.
- 609 Iken, A. (1981), The effect of the subglacialwater pressure on the sliding velocity of a
610 glacier in an idealized numerical model, *Journal of Glaciology*, 27, 407–421.
- 611 Iken, A., and R. A. Bindschadler (1986), Combined measurements of subglacial water pres-
612 sure and surface velocity of Findelengletscher, Switzerland: Conclusions about drainage
613 system and sliding mechanism, *Journal of Glaciology*, 32, 101–119.
- 614 James, T. D., T. Murray, N. E. Barrand, and S. L. Barr (2006), Extracting photogram-
615 metric ground control from lidar DEMs for change detection, *The Photogrammetric*
616 *Record*, 21(116), 312–328, doi:10.1111/j.1477-9730.2006.00397.x.
- 617 Jóhannesson, T. (2009), Propagation of a subglacial flood wave during the initiation of a
618 jökulhlaup, *Hydrological Sciences Journal*, 47:3, 417–434.
- 619 Kamb, B., C. F. Raymond, W. D. Harrison, H. Engelhardt, K. A. Echelmeyer,
620 N. Humphrey, M. M. Brugman, and T. Pfeffer (1985), Glacier Surge Mechanism:
621 1982–1983 Surge of Variegated Glacier, Alaska, *Science*, 227(4686), 469–479, doi:
622 10.1126/science.227.4686.469.
- 623 Kamb, B., H. Engelhardt, M. A. Fahnestock, N. Humphrey, M. Meier, and D. Stone
624 (1994), Mechanical and hydrologic basis for the rapid motion of a large tidewater
625 glacier: 2. Interpretation, *Journal of Geophysical Research*, 99(B8), 15,231–15,244, doi:
626 10.1029/94jb00467.
- 627 Krawczynski, M. J., M. D. Behn, S. B. Das, and I. Joughin (2009), Constraints on the
628 lake volume required for hydro-fracture through ice sheets, *Geophysical Research Letters*,

- 629 36(10), L10,501, doi:10.1029/2008gl036765.
- 630 Lindbäck, K., R. Pettersson, A. L. Hubbard, S. H. Doyle, D. van As, A. B. Mikkelsen,
631 and A. A. Fitzpatrick (2015), Subglacial water drainage, storage, and piracy be-
632 neath the Greenland Ice Sheet, *Geophysical Research Letters*, 42, 7606–7614, doi:
633 10.1002/2015gl065393.
- 634 Meier, M., S. Lundstrom, D. Stone, B. Kamb, H. Engelhardt, N. Humphrey, W. W. Dun-
635 lap, M. Fahnestock, R. M. Krimmel, and R. Walters (1994), Mechanical and hydrologic
636 basis for the rapid motion of a large tidewater glacier: 1. Observations, *Journal of*
637 *Geophysical Research*, 99(B8), 15,219–15,229, doi:10.1029/94jb00237.
- 638 Meierbachtol, T., J. Harper, and N. Humphrey (2013), Basal Drainage System Response
639 to Increasing Surface Melt on the Greenland Ice Sheet, *Science*, 341(6147), 777–779,
640 doi:10.1126/science.1235905.
- 641 MODIS Land Science Team (2015), MOD09 MODIS/Terra Surface Reflectance 5-Min
642 L2 Swath 250m, 500m and 1km, doi:10.5067/MODIS/MOD09.NRT.006.
- 643 Morlighem, M., E. Rignot, J. Mouginot, H. Seroussi, and E. Larour (2014), Deeply incised
644 submarine glacial valleys beneath the Greenland ice sheet, *Nature Geoscience*, 7(6),
645 418–422, doi:10.1038/ngeo2167.
- 646 Morriss, B. F., R. L. Hawley, J. W. Chipman, L. C. Andrews, G. A. Catania, M. J.
647 Hoffman, M. P. Lthi, and T. A. Neumann (2013), A ten-year record of supraglacial
648 lake evolution and rapid drainage in West Greenland using an automated processing
649 algorithm for multispectral imagery, *The Cryosphere*, 7(6), 1869–1877, doi:10.5194/tc-
650 7-1869-2013.

- 651 Mottram, R. H., and D. I. Benn (2009), Testing crevasse-depth models: a field
652 study at Breiamerjurökull, Iceland, *Journal of Glaciology*, 55(192), 746–752, doi:
653 10.3189/002214309789470905.
- 654 Nye, J. F. (1957), The Distribution of Stress and Velocity in Glaciers and Ice-Sheets,
655 *Proceedings of the Royal Society A: Mathematical, Physical and Engineering Sciences*,
656 239(1216), 113–133, doi:10.1098/rspa.1957.0026.
- 657 Oneel, S., K. Echelmeyer, and R. Motyka (2001), LeConte Glacier, Alaska, U.S.A., *Journal*
658 *of Glaciology*, 47(159), 567–578, doi:10.3189/172756501781831855.
- 659 Scott, J. B., A. M. Smith, R. G. Bingham, and D. G. Vaughan (2010), Crevasses triggered
660 on Pine Island Glacier, West Antarctica, by drilling through an exceptional melt layer,
661 *Annals of Glaciology*, 51(55), 65–70, doi:10.3189/172756410791392763.
- 662 Selmes, N., T. Murray, and T. D. James (2011), Fast draining lakes on the Greenland Ice
663 Sheet, *Geophys. Res. Lett.*, 38(15), L15,501, doi:10.1029/2011gl047872.
- 664 Shepherd, A., A. Hubbard, P. Nienow, M. King, M. McMillan, and I. Joughin (2009),
665 Greenland ice sheet motion coupled with daily melting in late summer, *Geophysical*
666 *Research Letters*, 36(1), L01,501, doi:10.1029/2008gl035758.
- 667 Shreve, R. L. (1972), Movement of water in glaciers, *Journal of Glaciology*, 11, 205–214.
- 668 Sole, A. J., D. W. F. Mair, P. W. Nienow, I. D. Bartholomew, M. A. King, M. J. Burke, and
669 I. Joughin (2011), Seasonal speedup of a Greenland marine-terminating outlet glacier
670 forced by surface melt-induced changes in subglacial hydrology, *Journal of Geophysical*
671 *Research: Earth Surface*, 116(F3), F03,014, doi:10.1029/2010JF001948.
- 672 Straneo, F., P. Heimbach, O. Sergienko, G. Hamilton, G. Catania, S. Griffies, R. Hallberg,
673 A. Jenkins, I. Joughin, R. Motyka, and et al. (2013), Challenges to understanding the dy-

- 674 namic response of Greenland's marine terminating glaciers to oceanic and atmospheric
675 forcing, *Bull. Amer. Meteor. Soc.*, *94*, 1131–1144, doi:10.1175/BAMS-D-12-00100.
- 676 Sundal, A., A. Shepherd, P. Nienow, E. Hanna, S. Palmer, and P. Huybrechts (2009),
677 Evolution of supra-glacial lakes across the Greenland Ice Sheet, *Remote Sensing of*
678 *Environment*, *113*(10), 2164–2171, doi:10.1016/j.rse.2009.05.018.
- 679 Tarboton, D. G. (1997), A new method for the determination of flow directions and
680 upslope areas in grid digital elevation models, *Water Resour. Res.*, *33*(2), 309–319,
681 doi:10.1029/96wr03137.
- 682 Tedesco, M., I. C. Willis, M. J. Hoffman, A. F. Banwell, P. Alexander, and N. S.
683 Arnold (2013), Ice dynamic response to two modes of surface lake drainage on the
684 Greenland ice sheet, *Environmental Research Letters*, *8*(3), 034,007, doi:10.1088/1748-
685 9326/8/3/034007.
- 686 Tweed, F. S., and A. J. Russell (1999), Controls on the formation and sudden drainage of
687 glacier-impounded lakes: implications for jökulhlaup characteristics, *Progress in Phys-*
688 *ical Geography*, *23*:1, 79–110.
- 689 van der Veen, C. J. (1998), Fracture mechanics approach to penetration of surface crevasses
690 on glaciers, *Cold Regions Science and Technology*, *27*(1), 31–47, doi:10.1016/s0165-
691 232x(97)00022-0.
- 692 van der Veen, C. J. (2007), Fracture propagation as means of rapidly transferring
693 surface meltwater to the base of glaciers, *Geophys. Res. Lett.*, *34*(1), L01,501, doi:
694 10.1029/2006gl028385.
- 695 Vaughan, D. (1993), Relating the occurrence of crevasses to surface strain rates, *Journal*
696 *of Glaciology*, *39*(132), 255–266.

697 Walder, J. S., and C. L. Driedger (1995), Frequent outburst floods from South Tahotna
698 Glacier, Mount Rainier, V.S.A.: relation to debris flows, meteorological origin and
699 implications for subglacial hydrology, *Journal of Glaciology*, *41:137*, 1–10.

Table 1. Thresholds and windows sizes used for pixel windows defined in MODIS imagery.

	Window Size (pixels)	Threshold
<i>L</i>	15 × 15	0.61
<i>W1</i>	15 × 15	0.80
<i>W2</i>	15 × 15	0.85
<i>W3</i>	12 × 12	0.80

Table 2. Thresholds and windows sizes used for pixel windows defined in MODIS imagery.

	Catchment Area (km ²)	Flow length (km)	
		Maximum	Mean
<i>L</i>	57	10.5	5.8
<i>W1</i>	33	11.5	4.4
<i>W2</i>	17	4.8	2.1
<i>W3</i>	24	7.2	2.7

Table 3. Parameter ranges and results from sensitivity testing of the model. The five percentiles are quoted as the difference in days between the modelled and observed date of hydrofracture, where negative values indicate earlier hydrofracture. Note that the order of ranges does not necessarily correspond to the order of the percentiles.

Parameter	Units	Range			Percentiles (days)				
		Lower	Base	Upper	5	25	50	75	95
Runoff factor	–	0.5	1	2	-7	-5	0	4	10
Tensile Stress	kPa	220	300	889	-2	-1	0	0	1
Critical Stress	kPa m ^{1/2}	10	150	400	0	0	0	1	1
Crevasse Width	m	0.1	1	2	-23	-13	-4	2	6
Spacing Ratio	–	0.1	1	1	0	0	1	1	1
Combined	–	As above			-15	-8	-1	6	16

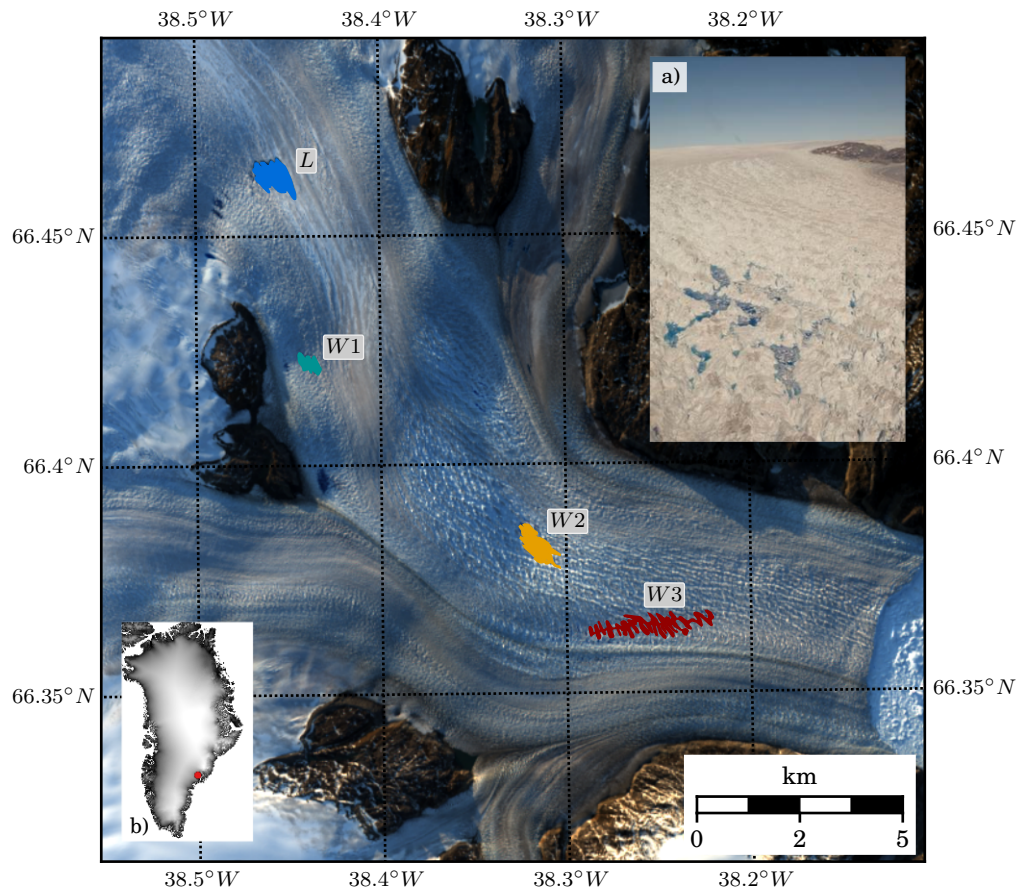


Figure 1. Locations of water areas monitored via remote sensing. Water areas L (blue), $W1$ (turquoise), $W2$ (orange), and $W3$ (red) are highlighted, colour-coding is consistent in subsequent figures. Background is a Landsat 8 image from 20th June 2014. Inset (a) photograph of $W2$. Inset (b) location of Helheim Glacier over GIMP surface DEM [Howat *et al.*, 2014].

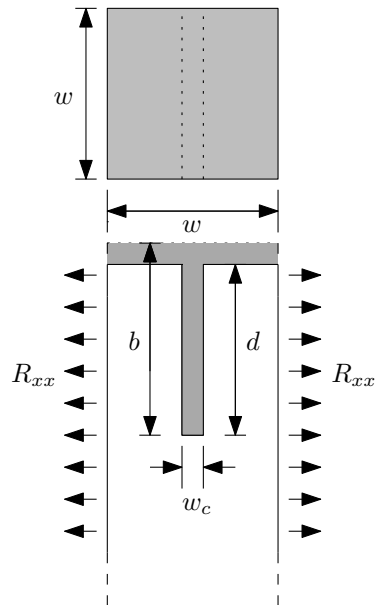


Figure 2. Crevasse geometry used to calculate water depth in LEFM modelling. Where, w is the width of a grid cell, w_c and d are the crevasse width and depth, respectively, and b is the resulting water depth.

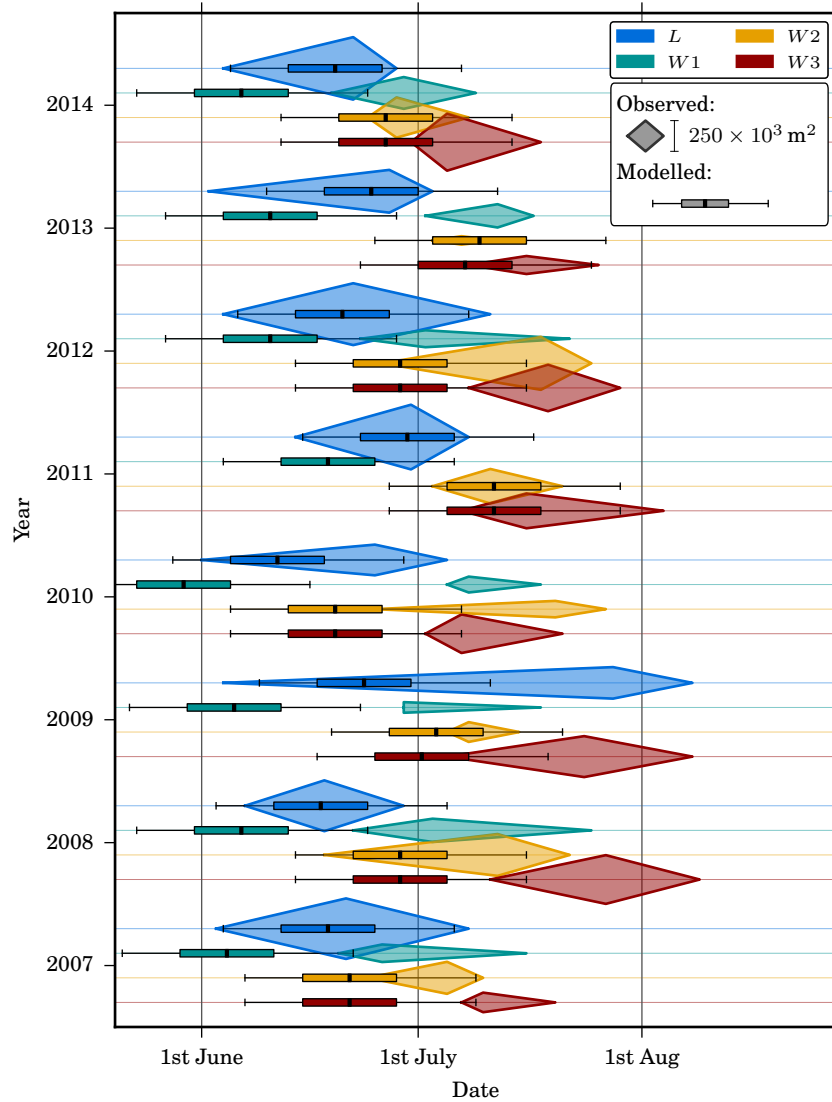


Figure 3. Results from remote sensing and modelling of surface water areas. Filled diamonds represent water areas derived from satellite imagery, where the maximum and minimum water areas have been picked and used to scale diamonds in the vertical. Box plots are used to represent the range of the modelled hydrofracture results, where the whiskers represent the 5th and 95th percentiles, and the box represents the first, second and third quartiles. Colours of diamonds and box plots correspond to colours of water areas used in Figure 1.

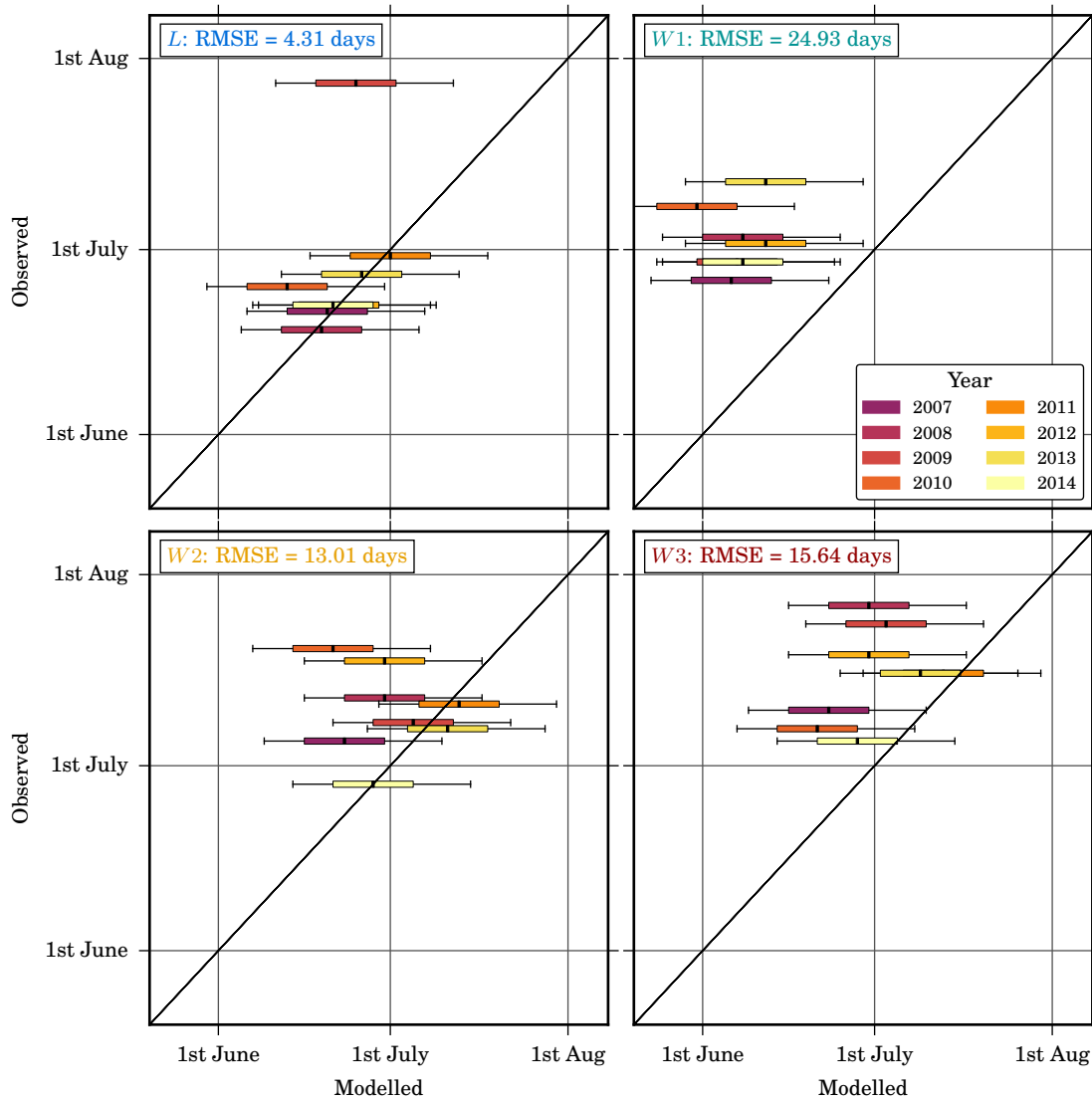


Figure 4. Modelled versus observed day of hydrofracture by area. Box plots are used to represent the range of the modelled hydrofracture results from sensitivity testing, where the whiskers represent the 5th and 95th percentiles, and the box represents the first, second and third quartiles. The black line represents a one-to-one relationship between the model and observations.

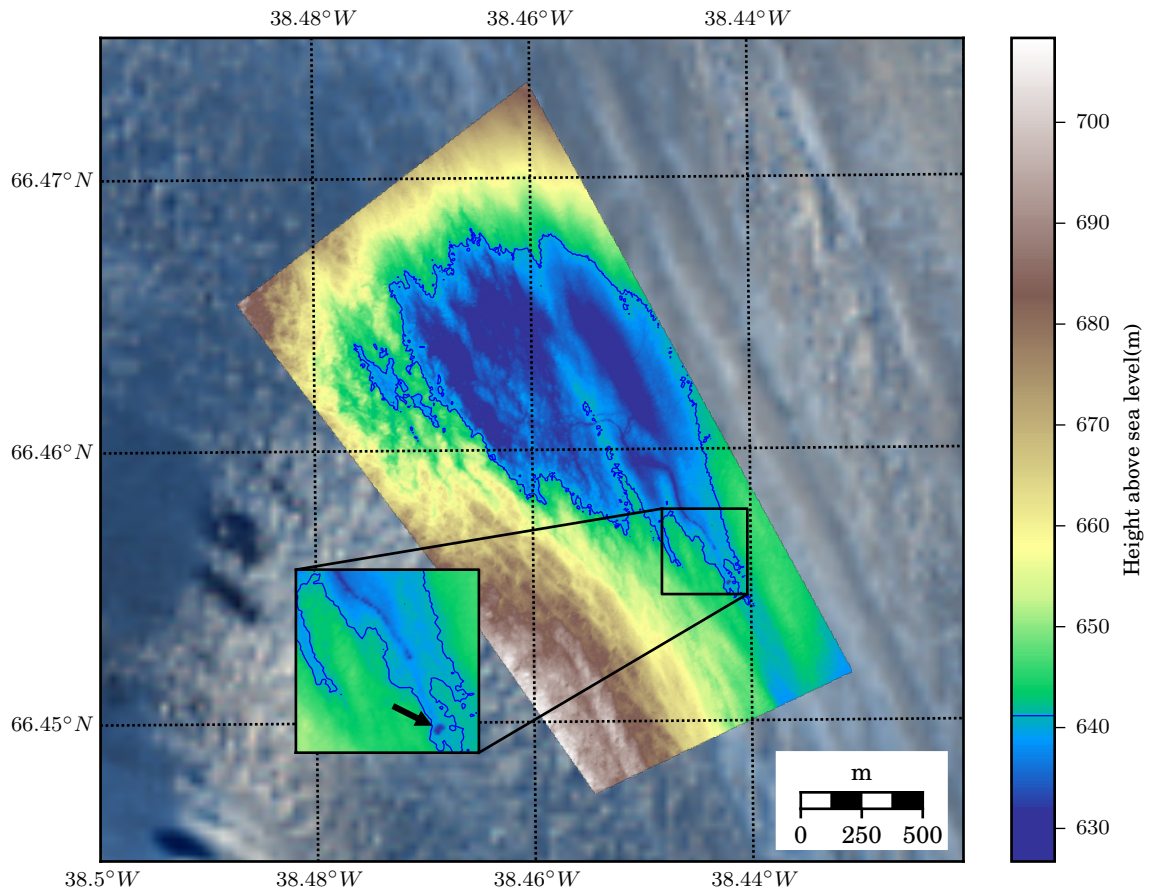


Figure 5. 5 m resolution DEM of the lake *L* produced from aerial photography collected in 2007. The maximum lake volume before over-topping is outlined in blue. The moulin is identified in the magnified image by the black arrow. Background is a Landsat 8 image from 20th June 2014.

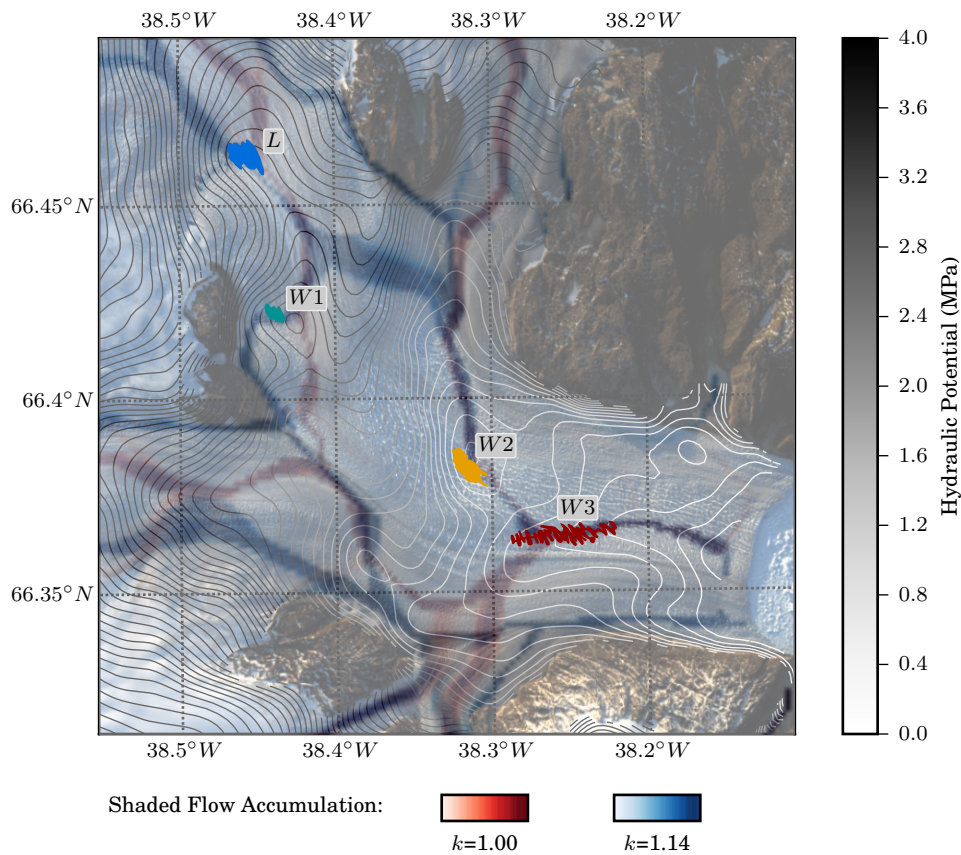


Figure 6. Contours of hydraulic potential, with shaded output of flow accumulation algorithm indicating flow routing at different values of k . Water areas are highlighted as for Figure 1. Background is a Landsat 8 image from 20th June 2014.